European Journal of Materials

ISSN: 2688-9277 (Online) Journal homepage: www.tandfonline.com/journals/tems20

Analyzing the effect of Fe on the microstructure and mechanical properties of a AA6008 alloy

Fazlollah Sadeghi, Nilam Barekar, Tungky Subroto, Pavel Shurkin, Geoff Scamans & Carla Barbatti

To cite this article: Fazlollah Sadeghi, Nilam Barekar, Tungky Subroto, Pavel Shurkin, Geoff Scamans & Carla Barbatti (2026) Analyzing the effect of Fe on the microstructure and mechanical properties of a AA6008 alloy, European Journal of Materials, 6:1, 2654912, DOI: 10.1080/26889277.2026.2654912

To link to this article: https://doi.org/10.1080/26889277.2026.2654912

Published online: 09 Apr 2026.

EUROPEAN JOURNAL OF MATERIALS
2026, VOL. 6, NO. 1, 2654912
https://doi.org/10.1080/26889277.2026.2654912

Taylor & Francis
by informa

CHARACTERIZATION AND MODELLING

OPEN ACCESS Check for updates

Analyzing the effect of Fe on the microstructure and mechanical properties of a AA6008 alloy

Fazlollah Sadeghi[a], Nilam Barekar[b], Tungky Subroto[b], Pavel Shurkin[a], Geoff Scamans[a,c] and Carla Barbatti[b,d]

[a]Brunel Centre for Advanced Solidification Technology (BCAST), Brunel University London, Uxbridge, Middlesex, UK; [b]Constellium University Technology Centre, Brunel University London, Uxbridge, Middlesex, UK; [c]Innoval Technology, Banbury, Oxfordshire, UK; [d]Constellium Technology Center, Voreppe Cedex, France

ABSTRACT

In this study, the effect of three different levels of iron impurity on the grain structure and texture of a recrystallized AA6008 alloy after extrusion was investigated. Microstructural examination was carried out to measure the microtexture, and the results were correlated with tensile and bending mechanical properties. Results demonstrated that number density of fragmented intermetallic particles after extrusion increases with increasing Fe content. They act as the nucleation sites of new grains, therefore refining the grain structure. Increasing Fe enhances Rotated Cube texture component at the periphery and the chance for surface crack during mechanical bending test. An increment of Fe-rich intermetallics on the other hand, leads to entrapment of Si solute reducing the free Si needed for precipitation hardening proven via thermodynamic calculations. The bending formability was found to correlate with the peripheral coarse grain structure as well as intermetallic particles.

ARTICLE HISTORY
Received 23 September 2025
Revised 20 February 2026
Accepted 30 March 2026

KEYWORDS
Al alloys; texture; recrystallization; cube texture; Fe-based intermetallics; hot extrusion

1. Introduction

Manufacturing of lightweight components by combination of direct chill (DC) casting of aluminium alloys followed by hot extrusion has proven to be a successful process route for both structural and transportation applications (Georgantzia et al., 2021; Miller et al., 2000; Sheppard & Sheppard, 1999). Among all classes of wrought aluminium alloy (AA) series, the AA6xxx Al-Si-Mg has been frequently used due to the combination of good extrudability, surface finish, and relatively high mechanical properties. The main application of this alloy class is in structural parts and outer body panels of automotive vehicles where high ductility allows the material to absorb energy during applied deformation processes such as car crash (Miller et al., 2000; Yang et al., 2024). Alloy properties are highly dependent on microstructural features such as grain structure and crystallographic texture.

From the chemical composition point of view, Mg_2Si precipitation is the main hardening mechanism for tailoring the microstructure to obtain desired mechanical properties (Jin et al., 2022; Yin et al., 2016). Other alloying elements also influence the final product properties. For instance, Mn, Cr, and Zr are mainly retained in solid solution after casting and precipitate during homogenization in the form of nano-sized precipitates, so-called dispersoids, preferably at the high-angle grain boundaries (HAGB) (Sheppard, 1999). Dispersoids hinder grain boundary migration during deformation at elevated temperatures, preventing grain growth. Fe, on the other hand, has a high tendency to form a variety of intermetallic (IMC) compounds with aluminium, Si, and Mn from the melt at the end of solidification (Cai, Jiang, et al., 2024; Cai, Song, et al., 2024; Que et al., 2018; 2022; Wu et al., 2014) due to a limited solubility in solid-state. The IMC particles cannot be dissolved in further heat treatment processes and are detrimental to the mechanical properties of various product components obtained by die-casting (Dong et al., 2019; Ji et al., 2013; Zhang et al., 2016) or extrusion (Karabay

CONTACT Fazlollah Sadeghi fazlollah.sadeghihosnijeh@brunel.ac.uk, dada.sadeghi@gmail.com Brunel Centre for Advanced Solidification Technology (BCAST), Brunel University London, Uxbridge, MiddlesexUB8 3PH, UK

et al., 2005; Pereira et al., 2018). It was claimed that Fe helps retain fibrous microstructure due to an increase in the dispersoids' fraction (Goik et al., 2023). Despite the high Mn content, stronger recrystallisation and grain growth were observed due to particle-stimulated nucleation (PSN) (Hovden et al., 2024; Österreicher et al., 2023). The Fe-based IMCs, particularly α-Al(FeMnCr)Si, can influence the texture during thermomechanical processes. By the accumulation of deformation in the surroundings of IMCs, a set of newly equiaxed grains possessing a texture that is deflected from the standard one can occur (Humphreys & Hatherly, 2012). PSN has been reported in cold-rolled AA8xxx (Kumar et al., 2023; Ryu & Lee, 2002), hot-extruded AA7xxx (She et al., 2019), rolled Al-Mg alloy (Aryshenskii et al., 2022), and high-temperature compressed Al-Cu-Li alloys (Wang et al., 2021).

Despite the vast applicability of AA6xxx series alloys and the necessity of using recyclable resources for sustainability purposes and reduction of carbon footprint, the effect of Fe addition as a single impurity element in recrystallised and fibrous alloys after hot extrusion has not been studied. For this purpose, the AA6xxx alloy with recrystallised grain structures is analysed in terms of the effect of single impurity Fe on the extruded profile texture, tensile and bending mechanical properties. Another similar analysis is published on the effect of Fe addition after hot extrusion of fibrous AA6110 and a comparative analysis is provided (Sadeghi et al., 2026).

2. Materials and methods

The standard AA6008, having a recrystallized microstructure, was used according to the International Aluminium Association (Alloys, 2018) for this study. Note that the absence of dispersoid-forming elements (Mn + Cr < 0.1 wt%) facilitates recrystallization after hot extrusion. Three variations of the AA6008 having Fe content of 0.2, 0.3, and 0.7 wt.% were DC cast into billets. Billets were then homogenized and extruded into flat strip profile as shown schematically in Fig. 1 in an industrial-scale extrusion press. The aim is to keep all influential process parameters and chemical composition constant (in the range of Cai et al., 2024) except for the level of Fe content. The alloy names of 0.2Fe, 0.3Fe, and 0.7Fe will be used for nomenclature of the alloys henceforth.

Firstly, the extruded samples were water quenched and stored for a few hours in floor ageing followed by immediately artificial ageing to T6 temper according to suggested cycles from the study by (Siddesh Kumar et al., 2022) to achieve maximum tensile strength. Then, samples were cut from the profile as shown schematically in Fig. 1 for characterisation. Tensile and bending tests were then performed on an Instron universal tensile machine following the standard procedures according to BS EN ISO 6892-1 (ASTM E8, 2010) and VDA 238-100 (V. 238–100, 2017). The bending test is performed in a 3-point bend test, where a sample supported on both sides is loaded at its centre point and bent to a specific angle or until the test sample fails. The average bending angle is then measured to report as a criterion of formability.

For microstructural examinations, the longitudinal cross-section of samples was prepared using standard metallographic procedures, polished, and anodized via 3% Barker solution at 15 V. To prepare the samples for EBSD, samples were polished using colloidal silica, followed by electropolishing using 30% nitric acid in methanol at −30 °C at 15 V to remove the residual surface strain. For EBSD analysis, a scanning electron microscope (SEM) (TESCAN Magna) was used at an accelerating voltage of 15 keV, 20 nA probe current, and 15 mm working distance to obtain electron back-scattered diffraction (EBSD) with a step size of 0.1 for mapping the data as well as energy

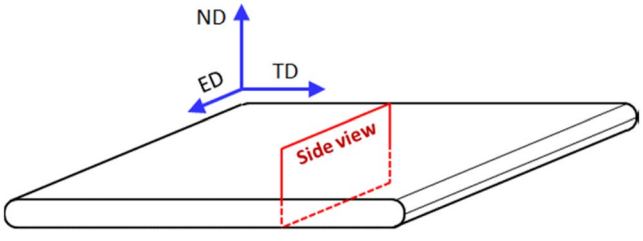

Figure 1. Schematic representation of extruded profile and sampling region from the side view.

dispersive spectroscopy (EDS). Extraction of the EBSD results was carried out using Oxford Aztec v6.0 and data acquisition using Aztec Crystal v3.1. TEM was used for observation of Nano-sized dispersoid particles. Samples were prepared by grinding thin specimens down to 100 µm followed by punching a 3 mm disk and jet polishing via Struers TenuPol-5 with the 25% nitric acid in methanol at −25 °C. The Talos F200i field emission transmission electron microscopy (FETEM) that operates at 200 keV and probe current of 0.030 nA was used equipped with EDS Bruker. Thermodynamic calculations were performed using Pandat software and PanAl2021 database based on non-equilibrium Scheil model.

Image analysis on the back scattered electron (BSE) images was performed using ImageJ software. The circularity of IMC particles is obtained according to Eq. 1 as shown in Fig. 2. The area (blue hatched) and perimeter (black perimeter line) are obtained from a binary image of each particle. Circularity of 1.0 represents a perfect circle and lower than 1.0 down to zero represents an irregular long shape.

$$Circularity = \frac{4\pi \times Area}{\left(Perimeter\right)^2} \quad \text{Eq. 1}$$

3. Results and discussion

3.1. Effect of iron on microstructure

The microstructures of the DC cast taken by optical microscopy (OM) of billet is shown in Fig. 3 to represent a general grain of cast microstructure having 125.9 ± 17.2 µm average grain size. A general SEM back scattered electron image (BSE) from the morphology of IMC particles at maximum iron content of 0.7Fe sample was also provided to compare the morphology of IMC particles in as-cast condition (Fig. 2b). The dark spots seen in Fig. 3a belong to the IMC phases which were confirmed by SEM. Under SEM-BSE image (Fig. 3b); however, they appear brighter due to the concentration of heavy elements (*i.e.*, Fe and Mn). Due to the extremely low solubility of Fe in Al matrix, homogenization treatment doesn't affect either shape or fraction of IMCs.

The overview picture of the profiles' microstructures after extrusion is shown in Fig. 4 which shows a recrystallized equiaxed grain structure. The coarse grains that are enucleated and grew at the profile surface, so called peripheral coarse grains (PCG), have strong contrast differences allowing them to distinguish between the grains, the bulk shows predominantly a monocontrast signifying a preferential texture. The difference between different recrystallized alloys is hardly seen due to poor contrast; therefore, EBSD tools will be used to quantify the corresponding effect of Fe.

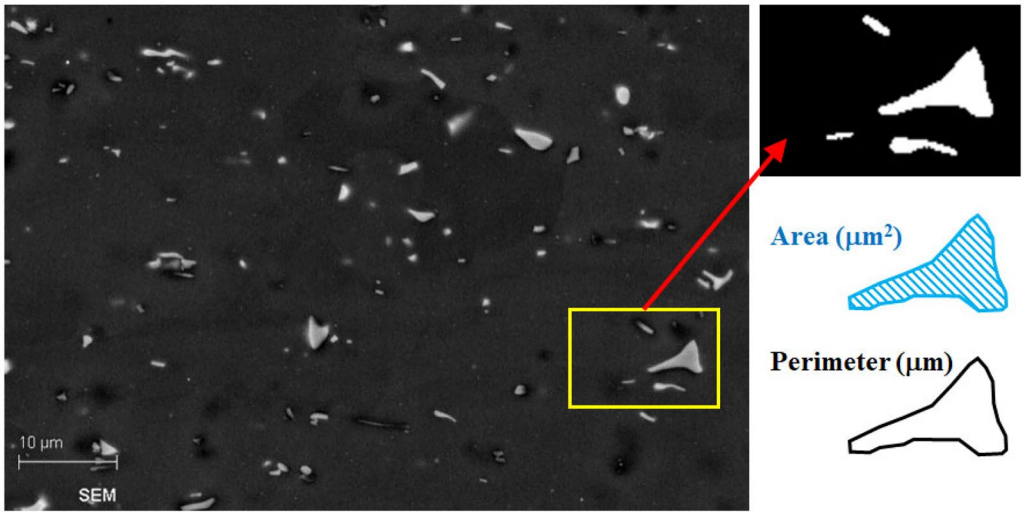

Figure 2. A sample representative of Fe-containing IMC particles analysis from BSE image of wrought Al alloys.

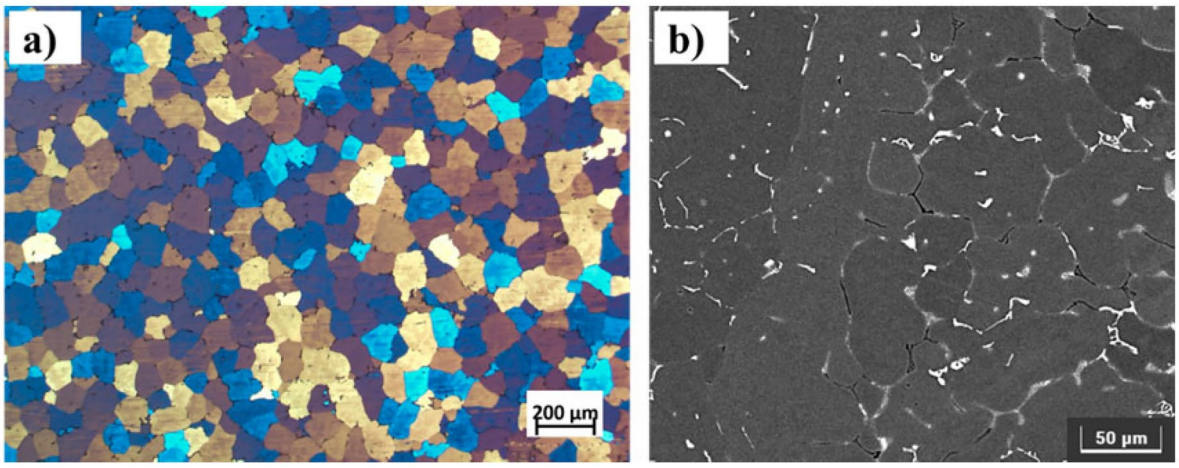

Figure 3. a) Anodized OM representative grain structure of DC cast billet to present the nominal grain structure and b) SEM-BSE image showing the distribution of Fe-based IMC particles.

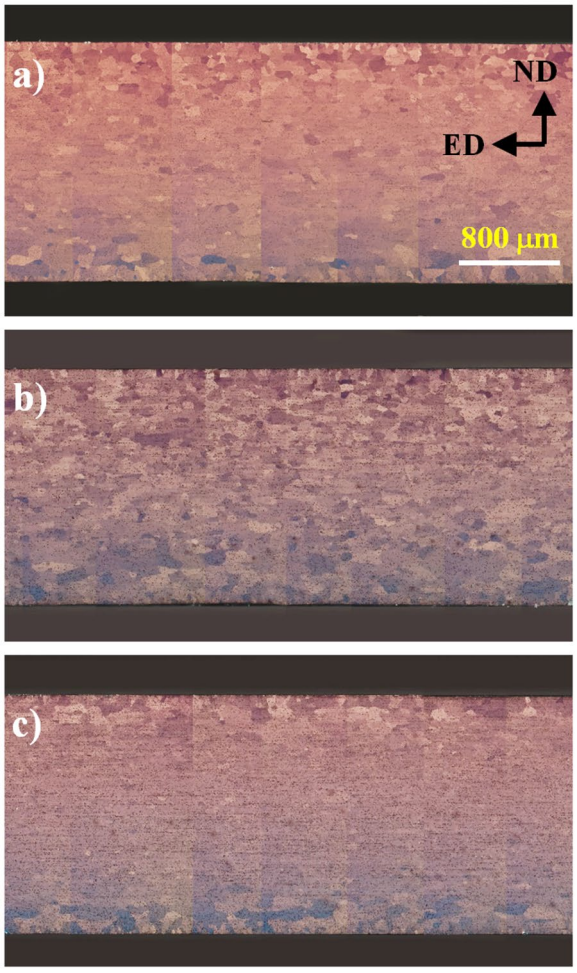

Figure 4. Optical microscopy images of AA6008 at a) 0.2Fe, b) 0.3Fe, and c) 0.7Fe extrudate profiles all at same magnification.

The formation of peripheral coarse grains at the extruded profile's surface (Kim et al., 2021; Negozio et al., 2024; Zhao et al., 2023) is influenced by chemical composition as well as process parameters. Goik et al. found that increasing Fe + Mn + Cr content resulted in a reduction in PCG thickness (Goik et al., 2023), but the effect of single iron addition was not studied. Apart from the effect of process

parameters, it has been reported that the existence of Mn as a dispersoid-forming element in an AA6082 alloy (Qian et al., 2019) results in precipitation of dispersoids increasing Zener-drag pressure and preventing recrystallisation. Based on optical microscopy observations, one can conclude that the recrystallized alloys do not change their nature due to an increase in Fe as the latter does not form pinning particles, and Mn content remains rather low. The EBSD analysis will help to quantify more precisely the differences in grain size and their orientations, which are determining factors for mechanical properties.

The effect of iron on the area fraction of IMC particles was investigated by analysis of the BSE images taken at the centre of profile thickness presented in Fig. 5. Visual inspection clearly shows an increasing trend in the Fe-based IMC particles along the extrusion direction by increasing Fe content due to an extremely low solubility of Fe in Al (Taylor, 2012). Due to a high contrast difference between Al matrix (dark grey) and Fe-IMC particles (white particles) in SEM-BSE images, quantifying the distribution of phases is feasible via image analysis. Thus, several images were taken for each condition and image analysis was performed using the ImageJ software to analyze the particles and corresponding area fraction histogram for each sample (Fig. 6a). It can be inferred that the size distribution of particles in 0.2Fe alloy (green graph in Fig. 6a) has a high area fraction at relatively small particle sizes whereas the peak intensity shifts toward bigger particle size values in case of 0.3Fe and 0.7Fe alloys (blue and red in Fig. 6a). This is a clear sign of IMC size increment by increasing Fe content.

A quantitative comparison between the area fraction, morphology, and circularity was carried out and plotted in Fig. 6b obtained from an average of 5 images at each condition. The IMCs were analyzed via BSE-SEM images of Fig. 5. The area fraction (which can be correlated with number density) of IMC particles increases with increasing Fe content; but the circularity remains the same. Minoda et al. have reported a similar trend in increasing size and number density of Fe-based IMC particles by increasing Fe content (Minoda et al., 2003). Due to the complexity of Fe-based IMC formation during solidification, and its inability to dissolve during any thermomechanical treatment, and processing (Taylor, 2004), the circularity of the IMCs does not regardless of any Fe content. Song et al. have made an attempt on the 3D observation of Fe-containing IMC particles after casting of recycling Al-Mg-Si alloys via synchrotron radiation facility and have visualized the structure of branched Chinese script morphology. Such a complex IMC morphology is broken during hot extrusion into irregular shape with much finer sizes.

A deep look into the single intermetallic particle after extrusion was also performed to investigate the type and crystal structure of IMC particles after the high temperature extrusion process. Fig. 7 presents a STEM image from IMC particles that are located at a grain boundary (GB) along with EDS mapping images of Mn, Fe, and Si (Fig. 7b–e). The atomic resolution STEM image confirms the simple cubic crystal structure of α-$Al_{15}(Fe,Mn)_3Si_2$ at ⟨111⟩ zone axes. This shows that all other types of IMC particles are transformed into α phase upon high-temperature treatment. Additionally, due to the brittle nature of intermetallic compounds with respect to the ductility of Al matrix, the accumulation of dislocations at the high-angle grain boundary (HAGB) can be witnessed in Fig. 7a.

According to the STEM image of Fig. 7, a faceted, blocky morphology can be witnessed located at the HAGB. Due to lack of dispersoid forming elements in recrystallized AA6008 alloy, the matrix is lacking any type of nano-sized dispersoid formation (Fig. 7a). The IMCs exhibit a characteristic

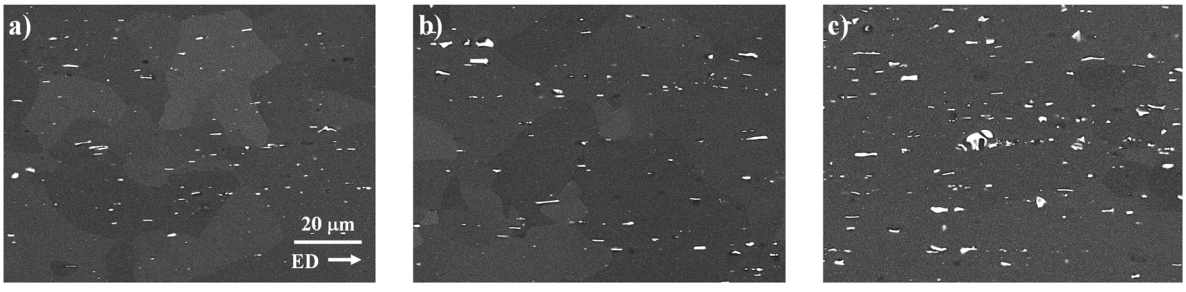

Figure 5. SEM/BSE images taken at the same magnification in AA6008 at a) 0.2Fe, b) 0.3Fe, and c) 0.7Fe alloys.

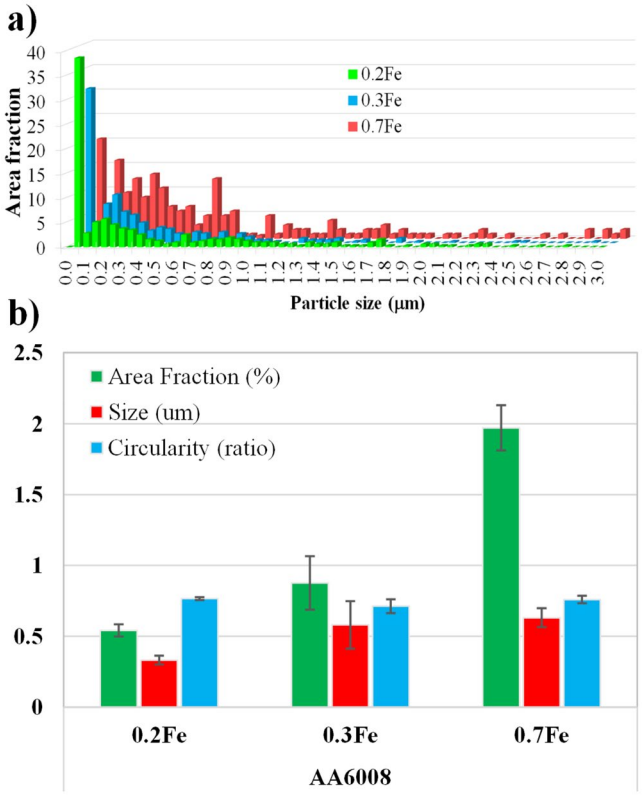

Figure 6. Statistical a) size distribution and b) area fraction, size, and circularity of Fe-based IMC particles analyzed from BSE images given in Fig. 3 at various Fe contents.

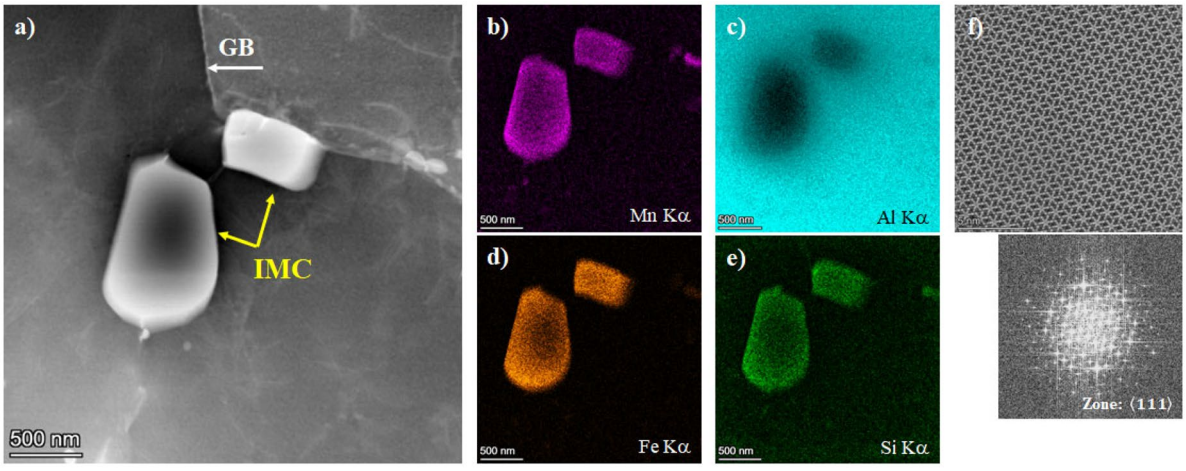

Figure 7. STEM image of two IMC particles closes to a high-angle grain boundary accompanied by the corresponding EDS mapping of b) Mn kα, c) Al kα, d) Fe kα, e) Si kα, and f) atomic resolution image of the particle at ⟨111⟩ zone axis and its FFT pattern.

contrast difference relative to the surrounding matrix, indicating an enrichment with elements having higher atomic number (*i.e.*, Fe and Mn) as presented in EDS mappings of Fig. 7b–e. EDS elemental mappings confirm that these particles are strongly enriched in Fe, Mn, and Si, while the surrounding matrix shows a comparatively homogeneous and lower signal intensity for these elements. The near-complete spatial overlap of Fe, Mn, and Si within the particles suggests the formation of a chemically well-defined α-$Al_{15}(Fe,Mn)_3Si_2$ intermetallic phase rather than elemental segregation or clustering. No evidence of elemental partitioning within individual particles is observed, implying a uniform internal composition. The preferential location of these IMCs at the HAGB is indicative of

possibility of PSN. Statistical grain size analysis provided in Fig. 12 will provide extra evidence of grain refinement by increasing Fe content. Such coarse and brittle Fe-based intermetallics are known to act as stress concentration site and may induce local strain at the adjacent Al matrix that facilitates new equi-axed grain nucleation and growth during high temperature deformation process (i.e., hot extrusion). At room temperature tensile test, IMC particles act as crack initiation sites, particularly when situated at grain boundaries.

To estimate the evolution of phases and composition by changing iron content of the AA6008, thermodynamic calculations were performed and presented in Fig. 8 based on the non-equilibrium Scheil model. Due to the absence of Mn in recrystallized alloy, the selection of Fe-rich intermetallic phases is $Al_{15}(Fe,Mn)_3Si_2$ and α-$Al_9Fe_2Si_2$ (Fig. 8a). As shown in the phase fraction calculations in Fig. 8b, with an increase in Fe content, the total fraction of Fe-based IMCs increases sharply, while the Si solute in the (Al) matrix decreases. This is noteworthy to mention that the Si in Al matrix is the available free Si dissolved in Al after some Si content is being consumed by Fe-based IMCs. This affects the precipitation hardening response which will be discussed later. Conclusively, it can be derived that the addition of iron in the alloy has contributed to the addition of Fe-rich IMCs as well as dispersoid precipitations when comparing thermodynamic calculations (Fig. 8) with experimental area fraction measurements (Fig. 6).

To evaluate the crystalline orientations corresponding to the grain structure in each investigated condition, EBSD analysis was performed over the whole cross-sections of all samples at a selected area as shown in IPF maps of the X-axis (Extrusion Direction - ED) in Fig. 9. It is noticeable that the microstructure of AA6008 is divided into the centre (bulk) and peripheral coarse regions (Fig. 9a–c). The central region has a dominant $\langle 001 \rangle \parallel ED$ orientation known as Cube texture.

To analyze the evolution of texture for each specific region of the cross-sectional EBSD data presented in Fig. 9, a representative orientation distribution function (ODF) map was obtained and presented for 0.2Fe condition of AA6008. The ODF maps were obtained by the FCC texture components that are summarized in Table 1.

In this alloy, mid-thickness (centre in bulk region) has a strong Cube texture that is the most dominant (Fig. 10a), followed by a rotated cube texture mainly in the peripheral region (Bertinetti et al., 2014; Cazacu et al., 2018). At the centre of profile, ODF indicates a sharp Cube texture ($\varphi_2 = 0°$) in Fig. 10a, which is a usual characteristic of fully recrystallized Al–Mg–Si alloys after extrusion and annealing simply due to the absence of nano-sized dispersoid particles. At the peripheral grains, texture is more randomized with much less intensity of Cube texture compared to the centre of thickness, yet a slight intensity of S texture can be observed ($\varphi_2 = 65°$) in Fig. 10f.

To quantify the effect of Fe addition on the microstructure and properties, each of the component fractions was calculated based on the texture components obtained from the EBSD maps (Fig. 9) and plotted in Fig. 11. It is evident that the R.Cube texture component increases by increasing Fe content accompanied by a slight reduction in the Cube recrystallisation component at the centre of

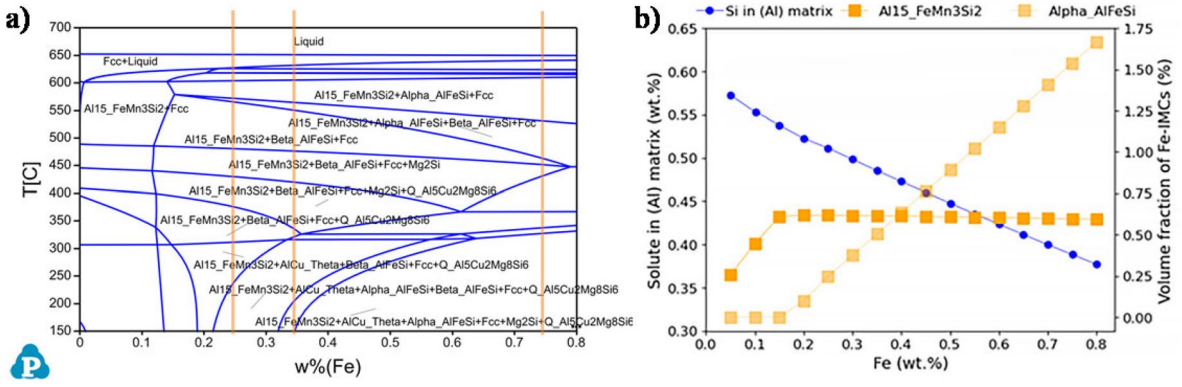

Figure 8. Thermodynamic a) pseudo-binary phase diagram calculations versus Fe content along with b) solute Si and Fe-based IMCs phase fraction calculations.

the thickness. Since the R.Cube is mostly observed at the periphery of the extruded specimen, it can be regarded as the PCG texture. Qualitatively, it appears that an increase in Fe content in the recrystallized alloy brought an increase in the depth of the peripheral grain zone (Fig. 11a–c) and amount of R.Cube from 17.7 to 22.5 and 31.1 for 0.2Fe, 0.3Fe, and 0.7Fe, respectively (Fig. 11d). A few grains with a texture different from Cube can be also found in the centre, but their size does not seem to change with increasing Fe content. Thus, considering the larger depth of the peripheral coarse grain zone, one can expect an influence on surface-sensitive properties such as bending (Elasheri et al., 2024; Snilsberg et al., 2010; Takeda et al., 2010).

Grain size refinement is another consequence of Fe addition as shown in Fig. 12 as the area fraction of large grains (over 200 µm) is less frequent by increasing iron content (e.g., 0.7Fe). The area-weighted average grain size data was measured from EBSD results based on ASTM E2627 considering HAGB ≥ 10°. Based on the average grain size values in Fig, 11, it is evident that the grain refinement has occurred in the centre part having Cube textured grains. The mechanism of grain refinement via Fe-based IMCs has been explained by Wang et al. (2023). They mentioned that particles having a diameter of more than 1 µm, mostly α-Al(FeMn)Si IMCs, have the potential to act as substrates for recrystallisation utilizing PSN (Hovden et al., 2024). One should point out the difference between dispersoids in pinning GBs with IMCs in grain refinement. According to Nes et al. (1985), the wrought microstructure contains two dominating structural particles within the matrix: the bimodal coarse particles (i.e., micro-sized Al(Fe,Mn)Si IMCs and coarse Mg_2Si particles; and fine particles

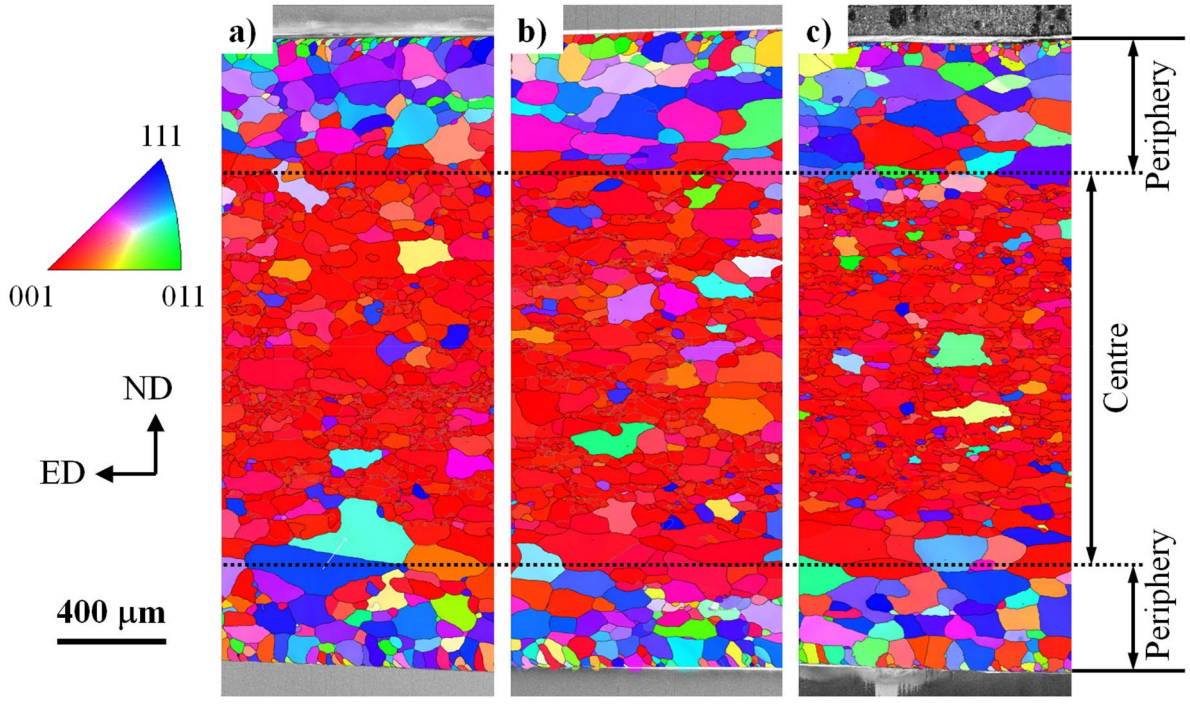

Figure 9. EBSD IPF maps from AA6008 at a) 0.2Fe, b) 0.3Fe, and c) 0.7Fe taken from the side view of the profiles where the extrusion direction is parallel to the X-axis. All images are at same magnification.

Table 1. Important recrystallized texture component with respect to each corresponding Euler Angles.

Texture Component		Orientation	Euler Angles		
			φ_1	Φ	φ_2
Recrystallisation fibre	Cube	$\{001\} \parallel \langle 100\rangle$; $\langle 100\rangle \parallel ED$	0/90	0	0/90
	R.Cube	$\{100\} \parallel \langle 011\rangle$; $\langle 110\rangle \parallel ED$	45	0	0
	Goss	$\{011\} \parallel \langle 100\rangle$	0	45	0/90
	S	$\{123\} \parallel \langle 634\rangle$	59	37	63
			52	74	33
			27	57	18

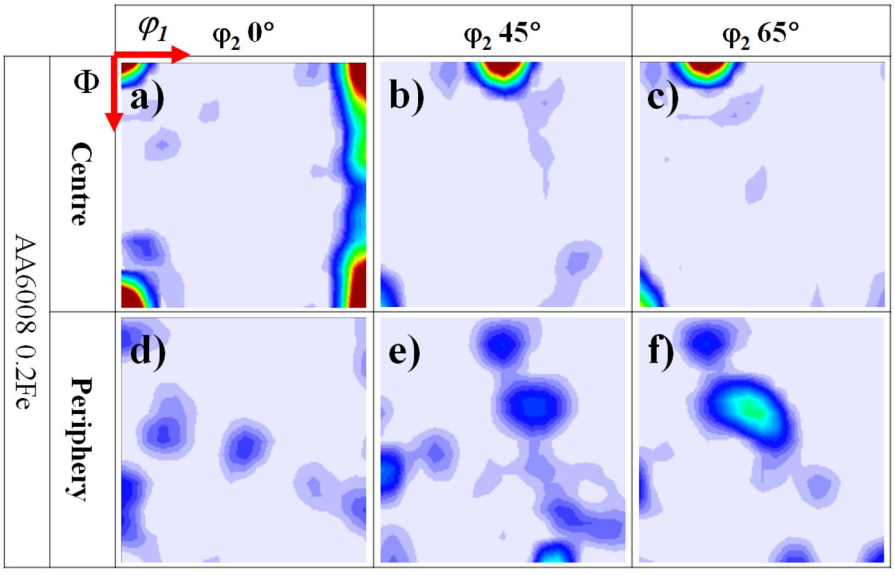

Figure 10. ODF maps calculated from each part of EBSD maps shown in Fig. 9 at (a, b, c) Centre and (d, e, f) periphery.

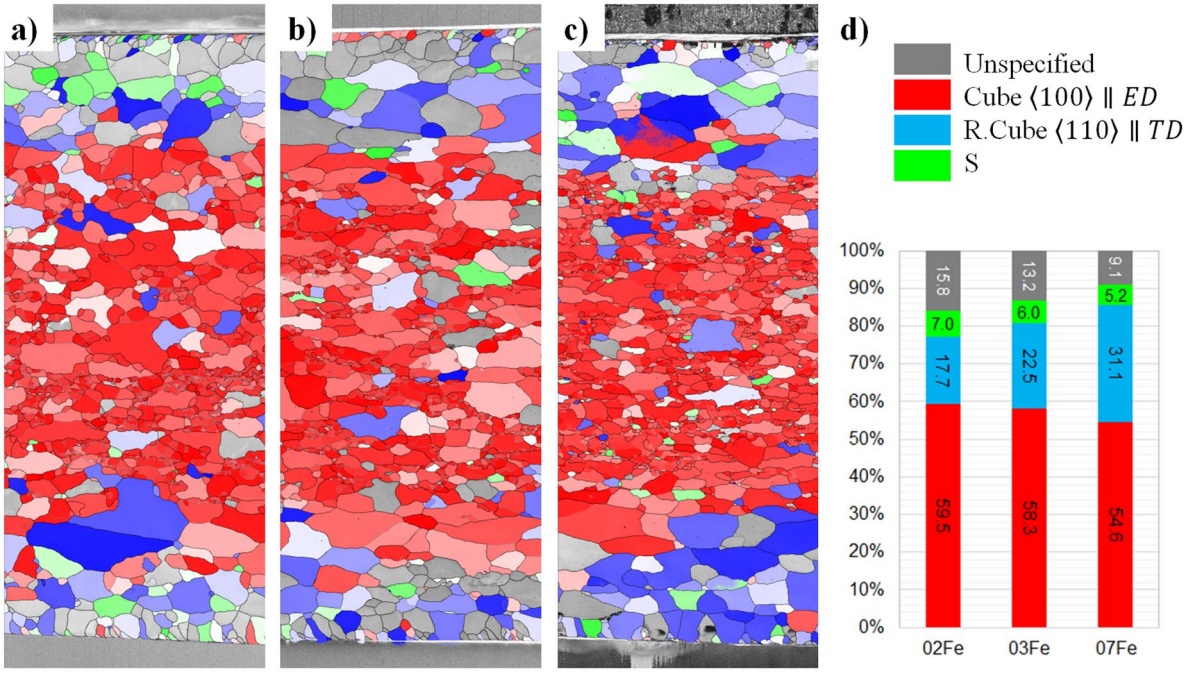

Figure 11. Texture components distribution map obtained from EBSD data at a) 0.2Fe, b) 0.3Fe, and c) 0.7Fe with d) quantitative fraction. All images have the same magnification.

(i.e., nano-sized Al(Fe,Mn)Si and Mg_2Si precipitates). The micro-sized particles promote recrystallisation through PSN that are recognised as the increment of the stored energy in the deformation zone around them. Since recrystallized alloy do not have a sufficient dispersoid forming element such as Mn and Cr, dispersoid precipitation does not play role in this study.

3.2. Effect of Fe on mechanical properties

The tensile properties shown in Fig. 13 show a reduction in yield strength (TYS) as well as ultimate tensile strength (UTS) by increasing Fe content. The effect of Fe in AA6xxx series has already been well-established (Sheppard, 1999). On one side, it has a high tendency to consume Si by forming β

(in cast structure) and α-$Al_{15}(Fe,Mn)_3Si_2$ (after homogenisation treatment) IMCs. Since Si provides a strengthening effect in both its solid solution and through the formation of Mg_2Si precipitates, reducing free Si will result in a reduction of precipitation hardening. This was proven via thermodynamic phase fraction calculation in Fig. 8b. Additionally, the formation of IMC particles has been said to affect mechanical properties by resisting deformation while the surrounding matrix deforms easily. The result is the formation of cracks from the broken IMC particles (Ji et al., 2013; Mathew et al., 2019; Österreicher et al., 2023; Song et al., 2022).

Bendability versus tensile properties is a valuable comparison for assessing the ductility of an engineering material for automotive applications. Results show that increasing iron content leads to a small ductility loss in Fig. 13c. Since the bendability of the material depends on the surface characteristics of the grains, peripheral grains and their texture components are important. This might be due to an increase in the R.Cube component of the PCG grains while its thickness does not alter considerably according to Fig. 11a–c. Our observations in Fig. 13b show that by increasing the iron content, the bending angle of the material decreases slightly at the same time as it experiences a slight tensile strength decrease. Firstly, an enhanced level of α-Al(FeMn)Si IMCs by increasing iron as shown in Fig. 5, quantitatively measured in Fig. 6, and thermodynamically calculated in Fig. 8. The IMC particles consume more Si resulting in less strengthening precipitates formation (*i.e.*, Mg_2Si) (Taylor, 2004; Minoda et al., 2003). Also, due to the undesirable recrystallisation texture that was observed at peripheral grains (as shown in Fig. 11), they cannot tolerate tension and compression on either side of the surface during bending resulting in loss of ductility and formation of crack that propagates through thickness.

Further analysis was performed on the bending tested samples using optical microscopy on the anodized samples presented in Fig. 14 at 0.2Fe, 0.3Fe, and 0.7Fe. The AA6008 reveals a dominant crack existing on the outer surface of the bent sample in all conditions. The grains located at the

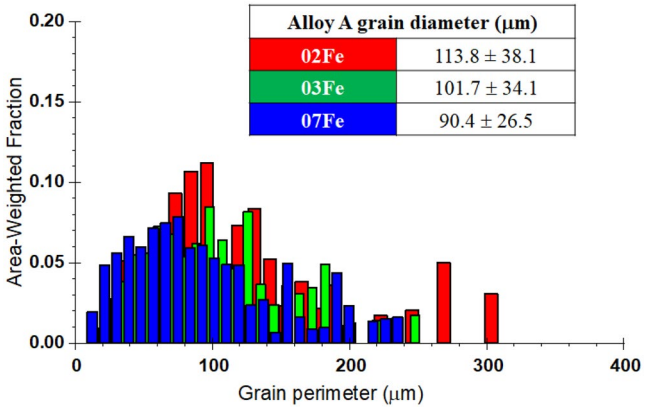

Figure 12. Grain size presentation in quantitative numeric and average weighted fraction

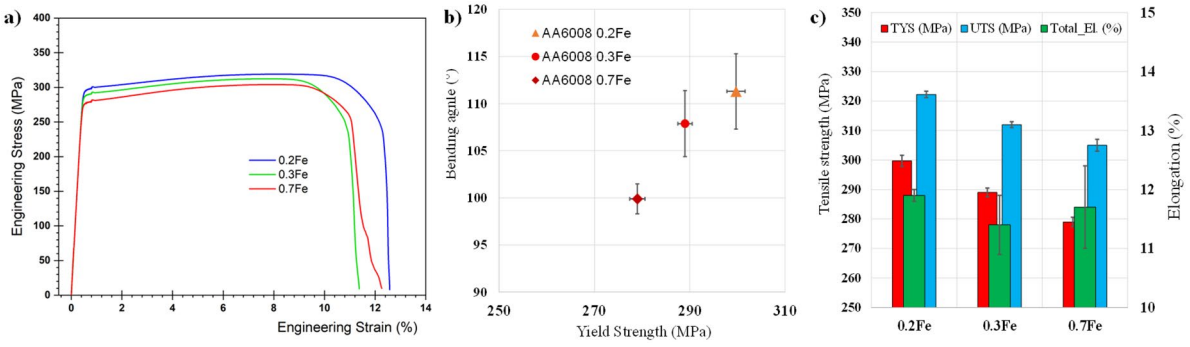

Figure 13. Result of mechanical a) tensile yield, ultimate strength, and total elongation and b) bending angle versus tensile yield strength having different Fe contents.

bottom of a specimen are also deformed in the form of compression. Grain refinement, as reported before in Fig. 11, is observed by increasing Fe content, too.

To further analyze the microstructure of bending-tested samples, the 0.7Fe sample was analyzed by low magnification EBSD to observe the grain structure in Fig. 15. The band contrast (BC) images (Fig. 15a) clearly demonstrate the abundance of deformation at both the compression and tension sides of the bent samples. The shear bands are accumulated at two opposite sides on the outer side, where tension is intensified (red arrows) as well as inner side, where compression is applied. Shear band formation is the response of the material to deformation (Takeda et al., 2010). The accumulation of shear bands followed by further applying deformation is the most suitable position for crack growth and failure (Elasheri et al., 2024). In addition, the grain boundaries possessing IMC particles are also prone to void formation as a result of boundary decohesion. Intergranular shear mechanism was explained by Ludtka et al. where void formation is facilitated at the grain boundary due to existence of precipitate free zone (Ludtka & Laughlin, 1982). This might be the reason for the start of crack formation and propagation from the coarse surface grains (PCG) in the form of intergranular fracture.

The GND map in Fig. 15c clearly justifies that strain localization at the outer face of the bending sample is accompanied by intergranular crack growth and local deformation of grains in between (Fig. 15b). Furthermore, the crystallography of each grain with respect to applied stress is responsible for activation of the slip system to further tolerate the deformation. Using a polycrystal-plasticity model, Bertinetti et al. (2014) have modelled both Cube and R.Cube textures to find out the difference in geometrical hardening as a factor for presenting formability. They have proven a difference between the geometrical hardening factor of grains having Cube or R.Cube textures. Comparing GND maps in

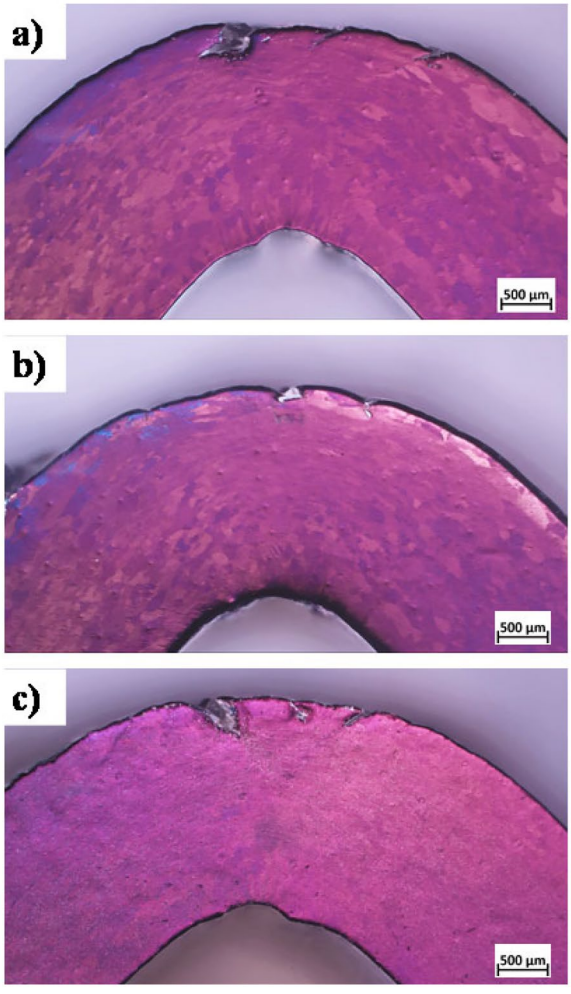

Figure 14. Optical microscopy anodized images at a) 0.2Fe, b) 0.3Fe, and c) 0.7Fe conditions.

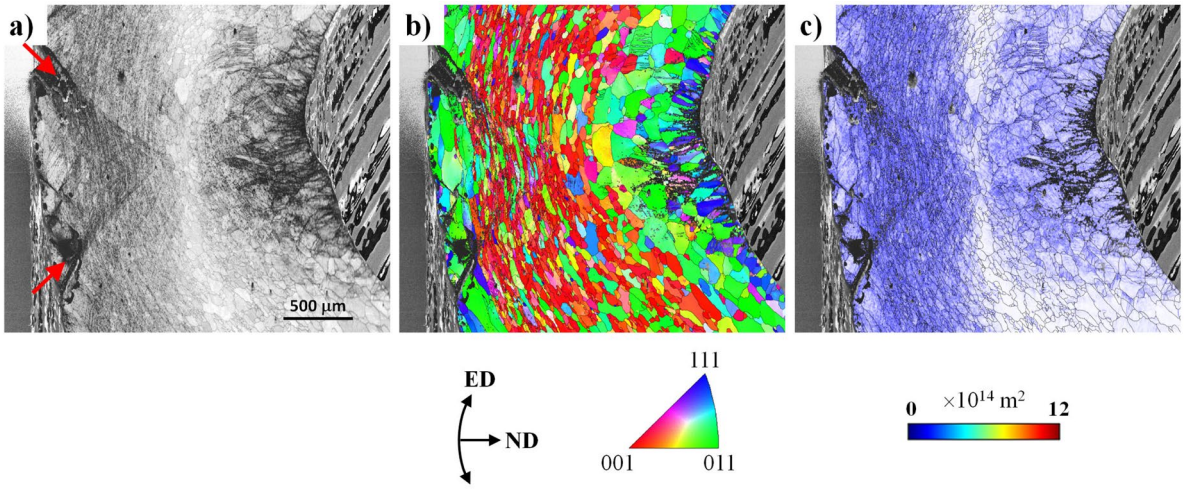

Figure 15. EBSD low magnification a) BC, b) IPF at TD (Z-axis), and c) GND maps at 0.7Fe content.

Fig. 15 and IPF maps in Fig. 9, it can be inferred that the PCG grains are less tolerant to the applied deformation relative to the central Cube textured grains acting as an initiation of failure during bending.

In conclusion, iron addition to AA6008 extrusion alloy can lead to a set of complex effects. From one perspective, it is obvious that the entrapment of part of the Si content in IMC particles leads to a decrease in precipitation hardening. Secondly, increasing Fe content alters the texture characteristics of peripheral grains A due to increasing macro-size IMC content. This happens through particle stimulated nucleation which has directly been observed in high Fe containing alloys of many other alloys such as AA8011 (Kumar et al., 2023), AA7055 (She et al., 2019), as well as through simulation (Radhakrishnan & Sarma, 2004). Thirdly, our TEM observations revealed the decoration of GBs with IMC particles that can weaken the cohesion of the boundary. This can act as a suitable place for crack propagation while applying external load in recrystallized peripheral grains with less favorable grain orientation. Finally, the shrinkage porosity formation around the IMC particles at the final stage of solidifications has been observed by Cai, Jiang, et al. (2024) and Cai, Song, et al. (2024). They have shown the deterioration of mechanical properties in the presence of shrinkage porosity. All these factors can facilitate the intergranular fracture and have a decremental effect on the mechanical properties of the alloy.

4. Conclusions

In this paper, the effect of single impurity iron addition on a recrystallized AA6008 grade was investigated from the viewpoint of microstructural and mechanical properties. The extruded flat strip profiles were analyzed by optical and electron microscopy before and after bending tests and the following conclusions were made:

- The addition of Fe increases the area fraction and size of the α-Al(Fe,Mn)Si intermetallic particles while it does not affect their morphology proven by thermodynamic calculation as well as image analysis.
- Fe addition contributes to reducing the Cube while increasing R.Cube texture. The thickness of peripheral grains is found to be relatively constant with increasing Fe content.
- An increase in the Fe content of the alloy led to increased intermetallic particles while refining grain size as well as reducing the free solute Si. The AA6008 alloy, nevertheless, satisfies performance requirements for the application, thus fulfilling the specification.

Acknowledgements

The author would like to appreciate the help and support from Constellium, UK.

Disclosure statement

No potential conflict of interest was reported by the authors.

References

Alloys, W. A. (2018). International alloy designations and chemical composition limits for wrought aluminum and wrought aluminum alloys, Alum. Assoc. Arlington, Virginia. ISSN: 2377 34. https://www.aluminum.org/teal-sheets

Aryshenskii, V., Grechnikov, F., Aryshenskii, E., Erisov, Y., Konovalov, S., Tepterev, M., & Kuzin, A. (2022). Alloying elements effect on the recrystallization process in magnesium-rich aluminum alloy. *Materials (Basel, Switzerland)*, *15*(20), 7062. https://doi.org/10.3390/ma15207062

ASTM E8 (2010). ASTM E8/E8M standard test methods for tension testing of metallic materials 1. *Annu. B. ASTM Stand*, *4*, 1–27. https://doi.org/10.1520/E0008

Bertinetti, M. A., Schwindt, C. D., & Signorelli, J. W. (2014). Effect of the cube orientation on formability for FCC materials: A detailed comparison between full-constraint and self-consistent predictions. *International Journal of Mechanical Sciences*, *87*, 200–217. https://doi.org/10.1016/j.ijmecsci.2014.05.031

Cai, Y. H., Jiang, G. D., Dong, J. L., Duan, B. B., Qiu, C., Zhang, W. W., & Zhang, D. T. (2024). Microstructure evolution and comprehensive properties of the extruded AA6008 crash-box profiles aged at 210 °C–220 °C. *Journal of Materials Research and Technology*, *28*, 3376–3384. https://doi.org/10.1016/j.jmrt.2023.12.244

Cai, Y., Song, D., Yang, D., Zhao, Y., Ke, B., Zhang, D., & Zhang, W. (2024). Effect of Na3AlF6 contents in refining flux on 3D characteristics of pore and mechanical properties of recycled Al-Mg-Si alloy. *Materials Today Communications*, *39*, 108797. https://doi.org/10.1016/j.mtcomm.2024.108797

Cai, Y., Song, D., Zhao, Y., Yang, D., Zhang, D., & Zhang, W. (2024). Effects of Fe content on the 3D morphology of Fe-rich phases and mechanical properties of cast Al-Mg-Si alloy. *Journal of Alloys and Compounds*, *990*, 174501. https://doi.org/10.1016/j.jallcom.2024.174501

Cazacu, O., Chandola, N., & Revil-Baudard, B. (2018). Analytical expressions for the yield stress and Lankford coefficients of polycrystalline sheets based on a new single crystal model. *International Journal of Material Forming*, *11*(4), 571–581. https://doi.org/10.1007/s12289-017-1366-3

Dong, X., Zhu, X., & Ji, S. (2019). Effect of super vacuum assisted high pressure die casting on the repeatability of mechanical properties of Al-Si-Mg-Mn die-cast alloys. *Journal of Materials Processing Technology*, *266*, 105–113. https://doi.org/10.1016/j.jmatprotec.2018.10.030

Elasheri, A., Parson, N., & Chen, X. G. (2024). Microstructure, tensile and bending properties of extruded Al–Mg–Si 6xxx alloys with individual and combined additions of Zr and Mn. *Mater. Sci. Eng. A*, *894*, 146156. https://doi.org/10.1016/j.msea.2024.146156

Georgantzia, E., Gkantou, M., & Kamaris, G. S. (2021). Aluminium alloys as structural material: A review of research. *Engineering Structures*, *227*, 111372. https://doi.org/10.1016/j.engstruct.2020.111372

Goik, P., Schiffl, A., & Höppel, H. W. (2023). Formation of peripheral coarse grain in thin-walled Al–Mg–Si extrusion profiles. *Metallurgical and Materials Transactions A*, *54*(10), 3940–3956. https://doi.org/10.1007/s11661-023-07144-3

Hovden, S., Kronsteiner, J., Arnoldt, A., Horwatitsch, D., Kunschert, G., & Österreicher, J. A. (2024). Parameter study of extrusion simulation and grain structure prediction for 6xxx alloys with varied Fe content. *Materials Today Communications*, *38*, 108128. https://doi.org/10.1016/j.mtcomm.2024.108128

Humphreys, F. J., & Hatherly, M. (2012). *Recrystallization and related annealing phenomena*. Elsevier.

Ji, S., Yang, W., Gao, F., Watson, D., & Fan, Z. (2013). Effect of iron on the microstructure and mechanical property of Al–Mg–Si–Mn and Al–Mg–Si diecast alloys. *Materials and Science Engineering A*, *564*, 130–139. https://doi.org/10.1016/j.msea.2012.11.095

Jin, H., Tie, D., & Guan, R. (2022). Precipitation behavior during re-aging of Al-Mg-Si-Cu alloy. *Materials and Design*, *220*, 110883. https://doi.org/10.1016/j.matdes.2022.110883

Karabay, S., Yilmaz, M., & Zeren, M. (2005). Investigation of extrusion ratio effect on mechanical behaviour of extruded alloy AA-6101 from the billets homogenised-rapid quenched and as-cast conditions. *Journal of Materials Processing Technology*, *160*(2), 138–147. https://doi.org/10.1016/j.jmatprotec.2004.05.025

Kim, S. B., Park, T. H., Kim, H. G., Lee, S. M., & Kim, H. K. (2021). The thickness of recrystallization layer and mechanical properties according to extrusion exit temperature. *Trans. Mater. Process*, *30*, 219–225.

Kumar, R., Ansari, N., Dandekar, T. R., & Khatirkar, R. K. (2023). Correlation of microstructure, texture and intermetallic particles during multi-step cross-rolling and annealing in a strip-cast AA8011 alloy. *Materials Today Communications*, *35*, 105812. https://doi.org/10.1016/j.mtcomm.2023.105812

Ludtka, G. M., & Laughlin, D. E. (1982). The influence of microstructure and strength on the fracture mode and toughness of 7XXX series aluminum alloys. *Metallurgical Transactions A*, *13*(3), 411–425. https://doi.org/10.1007/BF02643350

Mathew, J., Remy, G., Williams, M. A., Tang, F., & Srirangam, P. (2019). Effect of Fe intermetallics on microstructure and properties of Al-7Si alloys. *JOM Journal of the Minerals Metals and Materials Society*, *71*(12), 4362–4369. https://doi.org/10.1007/s11837-019-03444-5

Miller, W. S., Zhuang, L., Bottema, J., Wittebrood, A. J., De Smet, P., Haszler, A., & Vieregge, A. (2000). Recent development in aluminium alloys for the automotive industry. *Mater. Sci. Eng. A*, *280*(1), 37–49. https://doi.org/10.1016/S0921-5093(99)00653-X

Minoda, T., Uchida, H., Shibue, K., & Yoshida, H. (2003). Influence of iron content on mechanical properties of Al-Mg-Si alloy sheets. *Journal of Japan Institute of Light Metals*, *53*(11), 523–527. https://doi.org/10.2464/jilm.53.523

Negozio, M., Segatori, A., Pelaccia, R., Reggiani, B., & Donati, L. (2024). Experimental investigation and numerical prediction of the peripheral coarse grain (PCG) evolution during the extrusion of different AA6082 aluminum alloy profiles. *Materials Characterization*, *209*, 113723. https://doi.org/10.1016/j.matchar.2024.113723

Nes, E., Ryum, N., & Hunderi, O. (1985). On the Zener. *Acta Materialia*, *33*, 11–22.

Österreicher, J. A., Arnoldt, A. R., Gneiger, S., & Kunschert, G. (2023). Tolerance of Al–Mg–Si wrought alloys for high Fe contents: The role of effective Si. *Metallurgical and Materials Transactions A*, *54*(11), 4472–4480. https://doi.org/10.1007/s11661-023-07180-z

Pereira, L. H., Asato, G. H., Otani, L. B., Jorge, A. M., Kiminami, C. S., Bolfarini, C., & Botta, W. J. (2018). Changing the solidification sequence and the morphology of iron-containing intermetallic phases in AA6061 aluminum alloy processed by spray forming. *Materials Characterization*, *145*, 507–515. https://doi.org/10.1016/j.matchar.2018.09.006

Qian, X., Parson, N., & Chen, X. G. (2019). Effects of Mn addition and related Mn-containing dispersoids on the hot deformation behavior of 6082 aluminum alloys. *Mater. Sci. Eng. A*, *764*, 138253. https://doi.org/10.1016/j.msea.2019.138253

Que, Z., Wang, Y., & Fan, Z. (2018). Formation of the Fe-containing intermetallic compounds during solidification of Al-5Mg-2Si-0.7Mn-1.1Fe alloy. *Metallurgical and Materials Transactions A*, *49*(6), 2173–2181. https://doi.org/10.1007/s11661-018-4591-6

Que, Z., Wang, Y., Mendis, C. L., Fang, C., Xia, J., Zhou, X., & Fan, Z. (2022). Understanding Fe-containing intermetallic compounds in Al alloys: An overview of recent advances from the LiME research hub. *Metals (Basel)*, *12*(10), 1677. https://doi.org/10.3390/met12101677

Radhakrishnan, B., & Sarma, G. (2004). The effect of coarse non-deformable particles on the deformation and static recrystallization of aluminium alloys. *Philosophical Magazine*, *84*, 2341–2366. https://doi.org/10.1080/14786430410001689990

Ryu, J.-H., & Lee, D. N. (2002). The effect of precipitation on the evolution of recrystallization texture in AA8011 aluminum alloy sheet. *Materials and Science Engineering A*, *336*(1-2), 225–232. https://doi.org/10.1016/S0921-5093(01)01960-8

Sadeghi, F., Barekar, N., Subroto, T., Shurkin, P., Scamans, G., & Barbatti, C. (2026). Analyzing the effect of Fe on the microstructure and mechanical properties of a fibrous AA6110 Alloy. *Metals and Materials International*. https://doi.org/10.1007/s12540-025-02211-3

She, H., Shu, D., Dong, A., Wang, J., Sun, B., & Lai, H. (2019). Relationship of particle stimulated nucleation, recrystallization and mechanical properties responding to Fe and Si contents in hot-extruded 7055 aluminum alloys. *Journal of Materials Science and Technology*, *35*(11), 2570–2581. https://doi.org/10.1016/j.jmst.2019.07.014

Sheppard, T. (1999). *Processing of 6XXX alloys BT - Extrusion of Aluminium Alloys*. In T. Sheppard (Ed.) Springer US Boston, MA. pp. 253–322. https://doi.org/10.1007/978-1-4757-3001-2_6

Sheppard, T., & Sheppard, T. (1999). Metallurgical features affecting the extrusion of aluminium alloys BT. In T. Sheppard (Ed.), Extrusion of Aluminium Alloys. Springer US, Boston, MA. Pp. 69–126. https://doi.org/10.1007/978-1-4757-3001-2_3

Siddesh Kumar, N.M., Pramod, G.K., Samrat, P., Sadashiva, M., Dhruthi. (2022). A critical review on heat treatment of aluminium alloys, *Materials Today: Proceedings*. *58*, 71–79. https://doi.org/10.1016/j.matpr.2021.12.586

Snilsberg, K. E., Westermann, I., Holmedal, B., Hopperstad, O. S., Langsrud, Y., & Marthinsen, K. (2010). Anisotropy of bending properties in industrial heat-treatable extruded aluminium alloys. *Materials Science Forum*, *638-642*, 487–492. https://doi.org/10.4028/www.scientific.net/MSF.638-642.487

Song, D., Jia, Y., Li, Q., Zhao, Y., & Zhang, W. (2022). Effect of initial Fe content on microstructure and mechanical properties of recycled Al-7.0Si-Fe-Mn alloys with constant Mn/Fe ratio. *Materials (Basel, Switzerland)*, *15*(4), 1618, 1-12. https://doi.org/10.3390/ma15041618

Takeda, H., Hibino, A., & Takata, K. (2010). Influence of crystal orientations on the bendability of an Al-Mg-Si alloy. *Journal of Japan Institute of Light Metals*, *60*(5), 231–236. https://doi.org/10.2464/jilm.60.231

Taylor, J. A. (2004). *The Effect of Iron in Al-Si Casting Alloys* [Paper presentation]. 35th Aust. Foundry Inst. Natl. Conf., 148–157.

Taylor, J. A. (2012). Iron-containing intermetallic phases in Al-Si based casting alloys. *Procedia Materials Science*, *1*, 19–33. https://doi.org/10.1016/j.mspro.2012.06.004

V. 238–100 (2017). Test specification: Plate bending test for metallic materials, https://webshop.vda.de/VDA/en/vda-238-100-in-bearbeitungin-progress

Wang, X. Y., Jiang, J. T., Li, G. A., Wang, X. M., Shao, W. Z., & Zhen, L. (2021). Particle-stimulated nucleation and recrystallization texture initiated by coarsened Al2CuLi phase in Al-Cu-Li alloy. *Journal of Materials Research and Technology*, *10*, 643–650. https://doi.org/10.1016/j.jmrt.2020.12.046

Wang, Y., Yang, T., Lu, Q., Li, K., Wang, Z., & Du, Y. (2023). Grain size refinement and enhanced precipitation strengthening in a hot extruded 6xxx Al alloy without homogenization. *Materials Characterization*, *198*, 112718. https://doi.org/10.1016/j.matchar.2023.112718

Wu, Y., Liao, H., Yang, J., & Zhou, K. (2014). Effect of Si content on dynamic recrystallization of Al-Si-Mg alloys during hot extrusion. *Journal of Materials Science and Technology*, *30*(12), 1271–1277. https://doi.org/10.1016/j.jmst.2014.07.011

Yang, Z., Tang, J., Mo, X., Chen, W., Fu, D., Zhang, H., … Jiang, F. (2024). Microstructure, mechanical properties, and strengthening mechanisms of ultra-high strength Al-Zn-Mg-Cu alloy prepared by continuous extrusion forming process. *Materials and Design*, *242*, 112985. https://doi.org/10.1016/j.matdes.2024.112985

Yin, D., Xiao, Q., Chen, Y., Liu, H., Yi, D., Wang, B., & Pan, S. (2016). Effect of natural ageing and pre-straining on the hardening behaviour and microstructural response during artificial ageing of an Al-Mg-Si-Cu alloy. *Materials and Design*, *95*, 329–339. https://doi.org/10.1016/j.matdes.2016.01.119

Zhang, P., Li, Z., Liu, B., Ding, W., & Peng, L. (2016). Improved tensile properties of a new aluminum alloy for high pressure die casting. *Mater. Sci. Eng. A*, *651*, 376–390. https://doi.org/10.1016/j.msea.2015.10.127

Zhao, H., Sun, L., Zhao, G., Yu, J., Liu, F., Sun, X., … Cao, S. (2023). Abnormal grain growth behavior and mechanism of 6005A aluminum alloy extrusion profile. *Journal of Materials Science and Technology*, *157*, 42–59. https://doi.org/10.1016/j.jmst.2023.02.013